J. Fluid Mech. (1999), *vol.* 390, *pp.* 271–295. Printed in the United Kingdom

Near-critical reflection of internal waves

By THIERRY DAUXOIS† AND W. R. YOUNG

Scripps Institution of Oceanography, University of California at San Diego, La Jolla, CA 92093–0230, USA

(Received 3 August 1998 and in revised form 8 February 1999)

Using a matched asymptotic expansion we analyse the two-dimensional, near-critical reflection of a weakly nonlinear internal gravity wave from a sloping boundary in a uniformly stratified fluid. Taking a distinguished limit in which the amplitude of the incident wave, the dissipation, and the departure from criticality are all small, we obtain a reduced description of the dynamics. This simplification shows how either dissipation or transience heals the singularity which is presented by the solution of Phillips (1966) in the precisely critical case. In the inviscid critical case, an explicit solution of the initial value problem shows that the buoyancy perturbation and the alongslope velocity both grow linearly with time, while the scale of the reflected disturbance is reduced as $1/t$. During the course of this scale reduction, the stratification is 'overturned' and the Miles–Howard condition for stratified shear flow stability is violated. However, for all slope angles, the 'overturning' occurs before the Miles–Howard stability condition is violated and so we argue that the first instability is convective.

Solutions of the simplified dynamics resemble certain experimental visualizations of the reflection process. In particular, the buoyancy field computed from the analytic solution is in good agreement with visualizations reported by Thorpe & Haines (1987).

One curious aspect of the weakly nonlinear theory is that the final reduced description is a linear equation (at the solvability order in the expansion all of the apparently resonant nonlinear contributions cancel amongst themselves). However, the reconstructed fields do contain nonlinearly driven second harmonics which are responsible for an important symmetry breaking in which alternate vortices differ in strength and size from their immediate neighbours.

---

1. Introduction

1.1. *Reflection of internal waves on a sloping bottom*

Understanding the intensity and spatial distribution of turbulent vertical mixing in the ocean is an important problem in physical oceanography. Ocean models require accurate parametrizations of turbulent mixing to make realistic predictions of the transport of heat, salt and chemical species. Because the ocean is stably stratified, vertical mixing is inhibited and convection to great depth occurs only in restricted high-latitude regions. But the fluid which has reached the abyss by convection must ultimately return to the sea surface so as to maintain a quasi-steady state. How and where this return flow occurs remains obscure to this day. Munk (1966) and Armi

† Author to whom correspondence should be addressed: Laboratoire de Physique, ENS Lyon, 46 Allée d'Italie, 69007 Lyon, France (e-mail: Thierry.Dauxois@ens-lyon.fr).

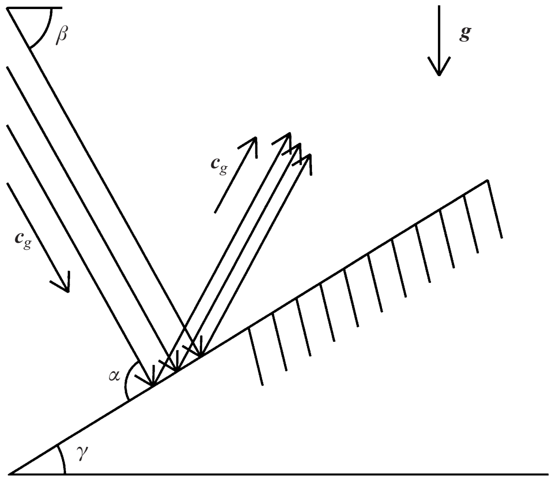

FIGURE 1. Schematic view of the reflection of the incident wave. The angle between the bottom slope and the horizontal is γ; the angle between the incident group velocity and the horizontal is β, and $\alpha = \beta + \gamma$. $\boldsymbol{c}_g$ indicates the group velocity and $\boldsymbol{g}$ indicates gravity.

(1978) suggested that significant vertical mixing takes place at sloping boundaries. Indeed, a recent report by Polzin *et al.* (1997) shows greatly elevated mixing rates above rough topography, especially in the deepest 150 m of the Brazil basin.

Sandstrom (1966) was the first to propose the oceanic internal wave field as a possible source of the energy which is needed to activate strong mixing near sloping boundaries. Internal waves are well documented in nature (see Munk 1981) and they obey simple, but unusual, reflection laws at a rigid boundary. In optics or acoustics, the incident and reflected wave rays make the same angle with respect to the normal to the reflecting surface, whereas for internal waves they make the same angle with respect to the direction of gravity. When internal waves reflect off a sloping bottom, the reflected wave has the same frequency ω as the incident wave. But because the wave frequency is related to the direction of propagation by $\omega = N \sin\beta$ preservation of ω implies preservation of the angle β (N is the buoyancy frequency and, as shown in figure 1, β the angle between the group velocity and the horizontal). This reflection law leads to a concentration of the energy density into a more narrow ray tube upon reflection. A fraction of the energy of the incident wave is radiated away as the reflected ray, but a part of the energy is lost due to turbulent dissipation, the rest being converted into irreversible mixing which accounts for the vertical transport of mass and matter.

Probably the most effective situation for boundary mixing arises when an oncoming wave reflects from a bottom slope which nearly matches the angle of wave propagation. At this critical angle, the analytic theory of internal waves reflecting from a uniformly sloping bottom (Phillips 1966) predicts that the reflected wave has infinite amplitude and infinitesimal wavelength. These unphysical results signal the failure of the idealizations (for example, linear waves and inviscid fluid) made by Phillips (1966).

Sandstrom (1966) reported observational evidence of energy enhancement at a particular frequency. Later Eriksen (1982, 1985) presented data showing energy and shear enhancement near the critical frequency at a few mooring sites. Eriksen interpreted deviations from a linear and inviscid theory as evidence for dissipation through shear instability and nonlinear interaction. The inviscid nonlinear case was theoretically considered by Thorpe (1987) who showed that singularities may occur at other frequencies when a finite-amplitude incident wave interacts resonantly with its own phase-locked reflected wave. Gilbert (1993) has also studied this phenomenon on the continental rise and slope off Nova Scotia. Energy enhancement at the critical frequency was significant at the 95% level for eight of the thirty tests performed even though the overall concavity of the slope should have slightly inhibited the phenomenon. Finally, Eriksen (1998) has recently reported striking observations made on the steep flank of a tall North Pacific Ocean seamount. Eriksen found a dramatic departures from the quasi-universal Garett–Munk spectral model near the bottom in a frequency band centred on the frequency for which ray and bottom slopes match.

1.2. *Laboratory and numerical experiments*

Following the first observational studies, Sandstrom (1966) performed a laboratory experiment that clearly demonstrated the amplification that results from internal wave reflection off a sloping bottom. Then, Cacchione & Wunsch (1974) showed that at the critical angle, the strong shearing motion becomes unstable and results in the formation of a series of periodic vortices. Overturning of these vortices produces mixed fluid that propagates into the interior as regularly spaced layers all along the slope.

Thorpe & Haines (1987) reported evidence of the three-dimensional structure of the boundary layer but they were unable to reproduce the formation of the vortex array seen by Cacchione & Wunsch (1974). The absence of vortices was also noted by Ivey & Nokes (1989) when they studied the mixing efficiency in the case of the breaking of a monochromatic incident wavefield uniformly distributed over the sloping bed. Taylor (1993) was particularly interested in the decaying turbulence and the mixing generated in the boundary layer. De Silva, Imberger & Ivey (1997) considered the case of a small ray width compared to the bed length.

Ivey & Nokes (1989), De Silva *et al.* (1997) and McPhee (1998) have also shown the formation of filaments by instabilities as waves approach the critical frequency by the action of the incident and reflected waves. Exactly at the critical angle, instead of producing fine-structured filaments, the waves produced turbulent vortices at the boundary. These vortices apparently mix boundary fluid which is presumably expelled along the isopycnal corresponding to the new density of the mixed fluid. As suggested by Caldwell, Brubaker & Neal (1978), these intrusive layers could also explain the presence of a highly 'stepped' temperature profile as the steep slope is approached at Lake Tahoe, California.

On the numerical side, Slinn & Riley (1996) have shown the creation of a thermal front moving upslope at the phase speed of the oncoming wave in the turbulent boundary layer. For a steep slope, the thermal front resembles a turbulent bore exhibiting nearly continuous localized mixing, whereas for shallower slope, the mixing is observed across the breadth of the domain and is temporally periodic. The internal wavefield continuously pumps fresh stratified fluid into the mixed layer, while simultaneously extracting the mixed boundary fluid. Slinn & Riley (1998*b*) have pursued their published work and have recently reported very detailed results on the effects of the slope angle on the turbulent layer thickness, mixing period and mixing efficiency. An advantage of the numerical approach is that it is possible to perform experiments over the shallow bottom slopes that are more typical of oceanic conditions.

Other recent numerical work of Javam, Imberger & Armfield (1997) showed that for near-critical waves, the instabilities were triggered at the bed, while for supercritical

	γ (deg.)	β (deg.)	$N \sin\beta$	h	a_0	$\tilde{Re}$	Re	a	ε	ϱ
Cacchione & Wunsch (1974)	30	30	0.48	40	0.4	2	5400	0.008	0.24	0.45
Thorpe & Haines (1987)	20	21	0.65	28	2.1	28	4500	0.037	0.32	0.13
Ivey & Nokes (1989)	30	30	0.30	40	4.6	139	3600	0.085	0.53	0.05
—	—	—	—	—	3.7	89	—	0.068	0.49	0.07
Taylor (1993)	20	20.1	0.16	53	3.2	14	4000	0.028	0.29	0.18
—	—	—	—	—	4.6	30	—	0.040	0.32	0.13
De Silva *et al.* (1997)	38	38	0.36	40	3.1	144	8200	0.052	0.61	0.03

TABLE 1. A summary of experimental parameters. γ is the angle between the bottom slope and the horizontal. $N \sin\beta$ the frequency in s^{-1}; h is the depth of water in cm; a_0 is the amplitude of the motion of the paddle in cm; $\tilde{Re} = \zeta^2 N \sin\beta/\nu$ is the Reynolds number defined by Thorpe & Haines (1987) and used by Ivey & Nokes (1989); $Re = N \sin\beta/\nu K^2$ is the Reynolds number defined by Slinn & Riley (1996) and us; a is the non-dimensional parameter defined in (2.12); $\varepsilon = (a \tan\alpha)^{1/3}$ is the small parameter used in our expansion and ϱ is the dissipative parameter defined in (3.8).

waves the instabilities develop away from the bed. Javam *et al.* (1997) also showed the nonlinear creation of harmonics.

1.3. *Questions and strategy*

Our goals in this paper are to understand the role of the nonlinearity in the reflection process, and to characterize the instabilities responsible for the transition to turbulence near the slope. We also emphasize the role of transience and dissipation in healing the singularity which occurs when the reflection is critical.

The paper is organized into four sections. The formulation of the problem is described first in § 2. We also present the main effect of the reflection process in the outer region. In § 3, we focus our study on the reflection problem in the boundary layer close to the slope. In § 4, we derive the explicit solution for the inviscid case, whereas the viscous effects are presented in § 5. Finally, § 6 contains the summary and conclusions.

2. Analysis

2.1. *Formulation in the coordinate system of the slope*

We will consider a two-dimensional, non-rotating, incompressible Boussinesq fluid, with constant Brunt–Väisälä frequency N and a uniformly sloping bed (angle of inclination is γ) shown in figure 1. We do not make the approximation of small inclination. In lakes, bed slopes are in the range 2°–20°, whereas in the ocean the r.m.s. slope of the sea bed is roughly 4°. In the vicinity of seamounts slopes can be considerably higher, in the range 6°–26° (see De Silva *et al.* 1997 and references therein). And most experiments use even larger angles of inclination.

The incident wave is a nearly monochromatic group of internal gravity waves. The angle between the incident group velocity and the horizontal is β and thus the carrier frequency of the group is $N \sin\beta$.

Our analysis employs a slope-oriented coordinate system in which x is the distance along the slope and z is the distance normal to the slope. In terms of these tilted coordinates the stratification of the Boussinesq fluid is

$$\rho = \rho_0 \left[1 - g^{-1}N^2(z\cos\gamma + x\sin\gamma) - g^{-1}b\right], \qquad (2.1)$$

where $b(x, z, t)$ is the buoyancy perturbation of the stratification at rest.

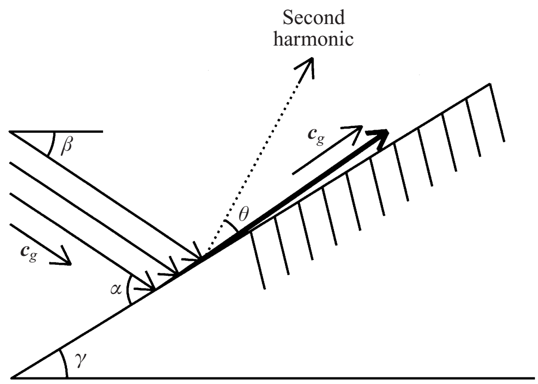

FIGURE 2. Schematic view of the reflection process for $\gamma \approx \beta$. The reflected wave is alongslope, whereas the nonlinearly reflected second harmonic, represented with the dotted line, makes an angle θ with the slope.

Denoting by (u, w) the components of the velocity field, the equations of motion are

$$\frac{\mathrm{D}u}{\mathrm{D}t} - \sin\gamma\, b + p_x = \nu\nabla^2 u, \tag{2.2a}$$

$$\frac{\mathrm{D}w}{\mathrm{D}t} - \cos\gamma\, b + p_z = \nu\nabla^2 w, \tag{2.2b}$$

$$\frac{\mathrm{D}b}{\mathrm{D}t} + N^2\sin\gamma\, u + N^2\cos\gamma\, w = \kappa\nabla^2 b, \tag{2.2c}$$

$$u_x + w_z = 0, \tag{2.2d}$$

where $\mathrm{D}/\mathrm{D}t = \partial_t + u\partial_x + w\partial_z$ is the convective derivative.

The boundary conditions at $z = 0$ are

$$u = w = 0, \quad N^2\cos\gamma + b_z = 0. \tag{2.3a–c}$$

The condition (2.3c) is that there is no diffusive flux of buoyancy through the slope. Wunsch (1970) and Phillips (1970) have shown that this condition at a sloping boundary produces a flow near the wall in a stably stratified fluid. Under laboratory conditions using dissolved salt this flow is very small (but detectable). This no-flux condition will cause some complications later.

2.2. *The incident wave and non-dimensional variables*

The situation we envisage is shown in figure 2. The incident wave nearly satisfies the critical condition that $\gamma = \beta$. Consequently the group velocity of the reflected wave makes a very shallow angle with the slope. The figure also anticipates some aspects of our analysis: when the reflection is nearly critical the advective term becomes important in a region near the slope. This quadratic nonlinearity results in the production of a second harmonic. This nonlinearly generated wave can then radiate away from the slope (see Thorpe 1987). The angle θ with which the second harmonic leaves the slope is not necessarily shallow.

Using the convention

$$u = -\psi_z, \quad w = \psi_x, \tag{2.4}$$

for the streamfunction, we consider an 'incident wave train'

$$[\psi, b] \approx [1, NK]A(t - sz)\cos(K\sin\alpha\, x + K\cos\alpha\, z - N\sin\beta t) \tag{2.5}$$

impinging on the slope. We have introduced the wavenumber K and, as suggested by figure 1,

$$\alpha \equiv \beta + \gamma. \tag{2.6}$$

The envelope, A in (2.5), changes slowly relative to the space and time scales of the carrier wave; s^{-1} is the vertical group velocity of this slowly modulated incident wave. Thus, near the slope, the incident wave switches on slowly with a prescribed amplitude $A(t)$.

We now non-dimensionalize (2.2) using the scales suggested by the incident wave in (2.5). The envelope can be written as

$$A = \psi_{\max}\hat{A}, \tag{2.7}$$

where $\psi_{\max}$ is the maximum amplitude of the streamfunction and so $\max(\hat{A}) = 1$. The non-dimensional variables are

$$[\hat{x}, \hat{z}] \equiv K[\sin\alpha\, x, \cos\alpha\, z], \quad \hat{t} \equiv N\sin\beta\, t, \tag{2.8a–c}$$

$$[\psi, u, w, b, p] \equiv \psi_{\max}[\hat{\psi},\ K\cos\alpha\ \hat{u},\ K\sin\alpha\ \hat{w},\ KN\hat{b},\ N\hat{p}]. \tag{2.8d–h}$$

Using the variables above, the non-dimensional equations of motion are

$$\frac{\mathrm{D}u}{\mathrm{D}t} + \frac{\tan\alpha}{\sin\beta}p_x - \frac{\sin\gamma}{\sin\beta\cos\alpha}\ b = \frac{1}{Re}\nabla^2 u, \tag{2.9a}$$

$$\frac{\mathrm{D}w}{\mathrm{D}t} + \frac{\cot\alpha}{\sin\beta}p_z - \frac{\cos\gamma}{\sin\beta\sin\alpha}\ b = \frac{1}{Re}\nabla^2 w, \tag{2.9b}$$

$$\frac{\mathrm{D}b}{\mathrm{D}t} + \frac{\sin\gamma\cos\alpha}{\sin\beta}\ u + \frac{\cos\gamma\sin\alpha}{\sin\beta}\ w = \frac{1}{Pe}\nabla^2 b, \tag{2.9c}$$

$$u_x + w_z = 0. \tag{2.9d}$$

The differential operators in (2.9) are

$$\nabla^2 = \sin^2\alpha\,\partial_x^2 + \cos^2\alpha\,\partial_z^2, \tag{2.10a}$$

$$\frac{\mathrm{D}}{\mathrm{D}t} = \partial_t + a\,(u\partial_x + w\partial_z)\,. \tag{2.10b}$$

In (2.9), we have dropped the 'hats' which would otherwise decorate the non-dimensional variables. The dimensionless dissipation parameters are the Reynolds and the Péclet numbers defined as follows:

$$Re = \frac{N\sin\beta}{\nu K^2} \quad \text{and} \quad Pe = \frac{N\sin\beta}{\kappa K^2}. \tag{2.11a,b}$$

The other non-dimensional parameter in (2.10*b*) is a measure of the nonlinearity:

$$a \equiv \frac{K^2\sin 2\alpha}{2N\sin\beta}\psi_{\max}. \tag{2.12}$$

Thorpe (1987) gives a useful physical interpretation of the amplitude parameter a: the maximum slope of the isopycnals in the incident wave (2.9) is $a\tan\beta/(1-a)$ if

$a < 1$ or infinite if $a > 1$. In what follows we will deal exclusively with the weakly nonlinear case in which a is small. The parameter a is also related to the internal Froude number $Fr \equiv \max(u_z/N)$ by

$$Fr = a\,\frac{\sin 2\beta \cos\beta}{\sin 2\alpha}. \tag{2.13}$$

Some authors prefer to use the minimal Richardson number $Ri \equiv Fr^{-2}$. Thus, with the appropriate geometric factors, a is simply related to the other measures of nonlinearity used in the literature.

In this non-dimensional and slope-oriented coordinate system, the dispersion relation of an inviscid linear internal wave (with all fields proportional to $\exp[\mathrm{i}kx + \mathrm{i}mz - \mathrm{i}\omega t]$) is

$$\omega = \pm\frac{k\sin\alpha\cos\gamma - m\cos\alpha\sin\gamma}{\sin\beta\sqrt{(k\sin\alpha)^2 + (m\cos\alpha)^2}}, \tag{2.14}$$

with the corresponding group velocity

$$\boldsymbol{c}_g = \left(\frac{\partial\omega}{\partial k}, \frac{\partial\omega}{\partial m}\right) = \pm\frac{\sin 2\alpha\,(m\cos\alpha\cos\gamma + k\sin\alpha\sin\gamma)}{2\sin\beta\left[(k\sin\alpha)^2 + (m\cos\alpha)^2\right]^{3/2}}(m, -k). \tag{2.15}$$

One solution of the dispersion relation (2.14) is $(\omega, k, m) = (1, 1, 1)$; this is the incident wave. In terms of the non-dimensional variables, the wave fields are

$$[\psi, b, p] = \frac{A}{2}\,\mathrm{e}^{\mathrm{i}(x+z-t)}\,[1, 1, -\mathrm{i}\cos\beta] + \text{c.c.} \tag{2.16}$$

where $A(t - sz)$ is the wave envelope and $s^{-1} = -\sin 2\alpha/2\tan\beta$ is the group velocity in the direction normal to the slope (put $k = m = 1$ in (2.15)).

2.3. *The 'near-critical' approximation*

We will develop a reductive approximation which is based on taking a distinguished limit in which a, $\beta - \gamma$, Re^{-1} and Pe^{-1} are all small. To motivate our scaling assumptions, we recall the classical solution of the reflection problem given by Phillips (1966). The no-flux boundary condition that $w = 0$ at $z = 0$ is satisfied by superposing a reflected plane wave on top of the incident wave in (2.16). In terms of non-dimensional variables, the vertical wavenumber of the reflected wave is

$$m = \frac{\tan(\gamma + \beta)}{\tan(\gamma - \beta)}. \tag{2.17}$$

The *critical reflection* condition is that $\beta = \gamma$ and then, according to (2.17), the wavenumber of the reflected wave is infinite. When $\gamma - \beta$ is small, m is large and the reflected wave has a much smaller length scale than that of the incident wave. This singularity, or near singularity, signals that the assumptions implicit in the Phillips' solution (stationarity, linearity and absence of dissipation) fail when the incidence is near critical.

We define the parameter ε by

$$\varepsilon \equiv (a\tan\alpha)^{1/3}. \tag{2.18}$$

(Because $a \propto \cos\alpha$, ε is bounded as $\alpha \to \pi/2$.) The reduction is based on the assumption that ε is small. As a measure of the degree to which the slope departs from the critical condition $\beta = \gamma$, we introduce σ defined

$$\beta = \frac{\alpha}{2} - \frac{\sigma\varepsilon^2}{2}, \quad \gamma = \frac{\alpha}{2} + \frac{\sigma\varepsilon^2}{2}. \tag{2.19a,b}$$

The sign of σ determines if the reflection is supercritical ($\sigma < 0$, upslope reflection); or subcritical ($\sigma > 0$, downslope reflection); $\sigma = 0$ corresponds to precisely critical reflection.

From (2.17) and (2.19a,b) it follows that when $\varepsilon \ll 1$,

$$m \approx \frac{\tan\alpha}{\sigma\varepsilon^2}. \tag{2.20}$$

Thus the 'near-critical' condition in (2.19a,b) ensures that the vertical wavenumber of the reflected wave is much greater than that of the incident wave.

Using (2.15), one can also show that the group velocity of the reflected wave in the near-critical case is

$$\boldsymbol{c}_g \approx \frac{\tan 2\beta}{\tan\beta}\frac{1}{m^2}[-m, 1]. \tag{2.21}$$

Using (2.20), one sees that the z-component of the group velocity in (2.21) is of order ε^4. Thus if $\varepsilon \ll 1$ it might take an impractically long time to establish the solution given by Phillips (1966).

The theory employs a matched asymptotic expansion in which the incident wave in (2.16) is in the *outer region* and the reflected disturbance is largely confined to an *inner region*, which is essentially a boundary layer close to the slope.

From (2.20), we can anticipate that as $\varepsilon \to 0$ a useful inner coordinate is likely to be $\xi = \varepsilon^{-2}\tan\alpha\, z$. The fields of the reflected wave are

$$[\psi, b, p] = \frac{A}{2}\,\mathrm{e}^{\mathrm{i}(x+mz-t)}\left[1, \frac{\sin(\beta+\gamma)}{\sin(\beta-\gamma)}, \mathrm{i}\cos\beta\right] + \text{c.c.} \tag{2.22}$$

and this suggests the introduction of the more appropriate variables $B = b\varepsilon^2/\sin\alpha$ and $P = p/\cos\beta$.

Using (2.21), we can also estimate the time for the reflected wave to travel through a distance on the order of its own wavelength. One finds that this transit time scales as ε^2 which motivates the introduction of a *slow timescale* $t_2 \sim \varepsilon^2 t$.

The other scaling assumptions are that

$$Re = \frac{\sin^2\alpha}{\varepsilon^6\nu_6} \quad \text{and} \quad Pe = \frac{\sin^2\alpha}{\varepsilon^6\kappa_6}. \tag{2.23a,b}$$

The main justification for the choices above is *a posteriori* – they work in the sense that the dissipative terms are comparable to the others in the final amplitude equation. Knowledge of ε is then the key to recovering a specific physical situation.

2.4. *Nonlinearly reflected second harmonic*

Because of the quadratic terms in (2.10b), one can anticipate, following Thorpe (1987), the nonlinear creation of a second harmonic in the small [$z = O(\varepsilon^2)$] region in which the advective terms become important. However this second harmonic does not remain confined to the region in which $z = O(\varepsilon^2)$. The second harmonic can radiate into the outer region where it appears as a plane wave. A successful completion of the matching problem requires that one recognizes this possibility that the inner region drives the outer region through this nonlinear process.

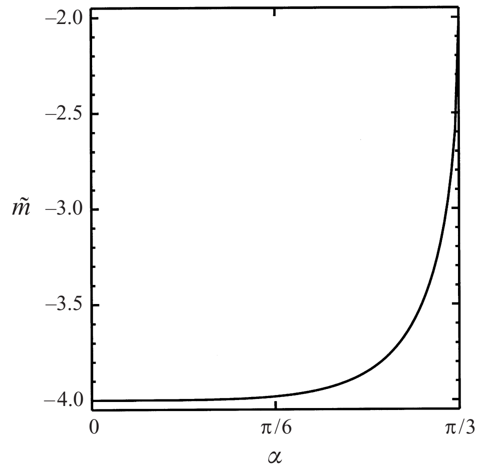

FIGURE 3. $\tilde{m}(\alpha)$, the z-wavenumber of the nonlinearly reflected second harmonic, in the near-critical case. When $\alpha > \pi/3$, $\tilde{m}(\alpha)$ is complex.

We now assemble the fields which describe the second harmonic in the outer region. A modulated plane wave second harmonic with upward group velocity is

$$[\psi, b, p] = \tfrac{1}{2} H \,\mathrm{e}^{\mathrm{i}(2x+\tilde{m}z-2t)}[1, \tilde{b}, \mathrm{i}\tilde{p}] + \text{c.c.}, \tag{2.24}$$

where $H(t - \tilde{s}z)$ is the envelope of the second harmonic and $\tilde{s}^{-1}$ is the vertical group velocity. The matching will determine H in terms of the incident amplitude A. In (2.24), we use the tilde to denote quantities associated with the second harmonic. In the nearly critical case these quantities are given to leading order by

$$\tilde{m}(\alpha) \equiv -\tfrac{2}{3} \operatorname{cosec} \tfrac{1}{2}\alpha \tan\alpha [\cos \tfrac{1}{2}\alpha + 2\,(2\cos\alpha - 1)^{1/2}], \tag{2.25a}$$

$$\tilde{b}(\alpha) \equiv 1 + \left(1 - \tfrac{1}{2}\tilde{m}\right)\cos\alpha, \tag{2.25b}$$

$$\tilde{p}(\alpha) \equiv (2\cos\alpha - 1)^{1/2}, \tag{2.25c}$$

$$\tilde{s}(\alpha) \equiv -\frac{\tan\alpha}{2} \frac{\left(4 + \tilde{m}^2 \cot^2\alpha\right)^{3/2}}{2 + \tilde{m}\cot\alpha\cot\tfrac{1}{2}\alpha}. \tag{2.25d}$$

If $\alpha > \pi/3$, the second harmonic is evanescent in z†, while for $\alpha < \pi/3$ the second harmonic propagates away from the slope; $\tilde{m}(\alpha)$ is plotted in figure 3. The angle θ between the slope and the direction of propagation of the second harmonic is

$$\theta = -\arctan\left(\frac{2\tan\alpha}{\tilde{m}(\alpha)}\right) \quad (\alpha \leqslant \pi/3). \tag{2.26}$$

Both θ and the group velocity $\tilde{s}^{-1}$ are shown in figure 4. Because both θ and the group velocity are non-zero the second harmonic is not trapped in a boundary layer close to the slope.

Slinn & Riley (1998*a*) have reported that when $\gamma < \pi/6$, intrusive layers form near the slope. However, interestingly, in the case $\gamma = \pi/6$ (i.e. the critical value above

† Javam *et al.* (1997) showed the nonlinear creation of evanescent harmonics. Apparently they never performed numerical experiments in the case $\gamma < \pi/6$ when they should propagate according to the present results.

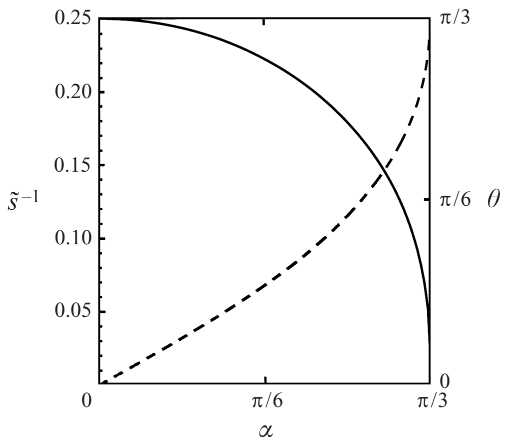

FIGURE 4. $\tilde{s}^{-1}$ (solid line), the z-component of the group velocity, and θ (dashed line) angle of reflection between the slope and the direction of propagation of the second harmonic in the critical case.

which the nonlinearly reflected second harmonic is evanescent), there is a uniform thickening of the dye layer along the slope.

2.5. *The outer region*

The first two orders of the outer solution are obtained by taking a combination of the incident wave in (2.16) and the second harmonic (2.24)

$$[\psi, b, p] = \tfrac{1}{2} A\, \mathrm{e}^{\mathrm{i}(x+z-t)}\, [1, 1, -\mathrm{i}\cos\beta] + \tfrac{1}{2}\varepsilon H\, \mathrm{e}^{\mathrm{i}(2x+\tilde{m}z-2t)} [1, \tilde{b}, \mathrm{i}\tilde{p}] + O(\varepsilon^2) + \text{c.c.} \quad (2.27)$$

The connection between $H(t-\tilde{s}z)$ and $A(t-sz)$ is determined by the matching problem in the inner region.

3. The inner region

In the inner region, we use a stretched coordinate ξ to describe the reflected disturbance close to the slope and a slow timescale t_2. Following our earlier discussion in § 2.3, these scales are

$$\xi \equiv \varepsilon^{-2} \tan\alpha\; z, \quad t_2 \equiv \mu\varepsilon^2 t, \qquad (3.1a, b)$$

where $\mu \equiv \cot(\alpha/2)$. As suggested by (2.22), we introduce

$$B \equiv \frac{\varepsilon^2 b}{\sin\alpha} \quad \text{and} \quad p \equiv \cos\beta\; P. \qquad (3.2a, b)$$

Finally, it is convenient to define

$$u \equiv \varepsilon^{-2} \tan\alpha\; U, \quad w \equiv W, \quad \psi \equiv \Psi, \qquad (3.3a\text{–}c)$$

so that we have

$$U = -\Psi_\xi \quad \text{and} \quad W = \Psi_x. \qquad (3.4a, b)$$

In the zone close to the slope, where $\xi = O(1)$, B and U are also $O(1)$. That is, the buoyancy perturbation and the alongslope velocity are $O(\varepsilon^{-2})$ larger than in the incident wave.

In the inner region, using (2.23a,b), (2.9) becomes

$$\frac{\mathrm{D}U}{\mathrm{D}t} - B = \varepsilon^2\left[-\mu P_x + \mu\sigma B + \nu_6 U_{\xi\xi}\right] + O(\varepsilon^3), \tag{3.5a}$$

$$-P_\xi + B = \varepsilon^2\left[\frac{\sigma}{2\mu}B + \frac{1}{\mu}\frac{\partial W}{\partial t}\right] + O(\varepsilon^3), \tag{3.5b}$$

$$U_x + W_\xi = 0, \tag{3.5c}$$

$$\frac{\mathrm{D}B}{\mathrm{D}t} + U = \varepsilon^2\left[-\mu\sigma U - \mu W + \kappa_6 B_{\xi\xi}\right] + O(\varepsilon^3), \tag{3.5d}$$

where the convective derivative is

$$\frac{\mathrm{D}}{\mathrm{D}t} = \partial_t + \mu\varepsilon^2\partial_{t_2} + \varepsilon\left(U\partial_x + W\partial_\xi\right). \tag{3.6}$$

Using the complex variable $S = \Psi + \mathrm{i}P$, (3.5) can be written compactly as

$$S_{\xi t} - \mathrm{i}S_\xi = -\varepsilon J(\Psi, S_\xi) + \varepsilon^2\Big[-\mu S_{\xi t_2} + \mathrm{i}\mu\left(\sigma S_\xi - S_x\right) - \frac{\mathrm{i}}{\mu}\left(W_{tt} - \mathrm{i}W_t\right) - \frac{\mathrm{i}\sigma}{2\mu}\left(B_t - \mathrm{i}B\right) + \mu\varrho^2 S_{\xi\xi\xi} + \mu\zeta S^*_{\xi\xi\xi}\Big] + O(\varepsilon^3), \tag{3.7}$$

where

$$\varrho^2 = \frac{\nu_6 + \kappa_6}{2\mu}, \quad \zeta = \frac{\nu_6 - \kappa_6}{2\mu}, \tag{3.8a,b}$$

and $J(a, b)$ is the Jacobian.

The equation above must be solved with the boundary conditions:

$$S(x,0,t,t_2) + S^*(x,0,t,t_2) = 0 \quad \text{(no normal flow)}, \tag{3.9a}$$

$$S_\xi(x,0,t,t_2) + S^*_\xi(x,0,t,t_2) = 0 \quad \text{(no slip)}, \tag{3.9b}$$

$$S_{\xi\xi}(x,0,t,t_2) - S^*_{\xi\xi}(x,0,t,t_2) = 0 + O(\varepsilon^4) \quad \text{(no flux of buoyancy)}. \tag{3.9c}$$

By taking the inner limit of the right-hand side of (2.27), we obtain the matching condition

$$\lim_{\xi\to\infty} S = A(t_2)\mathrm{e}^{\mathrm{i}(x-t)} + \varepsilon H(t_2)\frac{(1-\tilde{p}\sec\beta)}{2}\mathrm{e}^{-2\mathrm{i}(t-x)} + \varepsilon H^*(t_2)\frac{(1+\tilde{p}^*\sec\beta)}{2}\mathrm{e}^{2\mathrm{i}(t-x)} + O(\varepsilon^2). \tag{3.10}$$

The weakly nonlinear analysis proceeds by introducing not only slow space and time scales but also seeking a solution of (3.7) in terms of the regular perturbation expansions

$$S = S_0 + \varepsilon S_1 + \varepsilon^2 S_2 + O(\varepsilon^3). \tag{3.11}$$

Substituting (3.11) into (3.7) leads to the following hierarchy:

$$\varepsilon^0: \quad (\partial_t - \mathrm{i})\,\partial_\xi S_0 = 0, \tag{3.12a}$$

$$\varepsilon^1: \quad (\partial_t - \mathrm{i})\,\partial_\xi S_1 = -J(\Psi_0, S_{0\xi}), \tag{3.12b}$$

$$\varepsilon^2: \quad (\partial_t - \mathrm{i})\,\partial_\xi S_2 = -\left[J(\Psi_0, S_{1\xi}) + J(\Psi_1, S_{0\xi})\right] + [LT]_0. \tag{3.12c}$$

In (3.12c), $[LT]_0$ means the linear term in the square bracket of the right-hand side of (3.7), evaluated with S_0.

3.1. *Leading order*

From (3.12a), we obtain the leading-order solution

$$S_0 = \mathrm{e}^{-\mathrm{i}(x-t)}\mathscr{S}(\xi, t_2) + A\mathrm{e}^{\mathrm{i}(x-t)} - A^*\mathrm{e}^{-\mathrm{i}(x-t)}, \tag{3.13}$$

and the leading-order streamfunction

$$\Psi_0 = \tfrac{1}{2}\mathrm{e}^{\mathrm{i}(t-x)}\mathscr{S}(\xi, t_2) + \text{c.c.} \tag{3.14}$$

The evolution of $\mathscr{S}(\xi, t_2)$ will be determined at higher order. However, at this order, the matching (3.10) is satisfied provided that

$$\lim_{\xi\to\infty} \mathscr{S} = A^*, \tag{3.15}$$

whereas the no-flux and no-slip condition at $\xi = 0$ requires that

$$\mathscr{S}(0, t_2) = \mathscr{S}_\xi(0, t_2) = \mathscr{S}_{\xi\xi}(0, t_2) = 0. \tag{3.16}$$

Equation (3.13) is not the most general solution of (3.12a). However, for simplicity we include only the $\mathrm{e}^{-\mathrm{i}x}$ harmonic which is required by the matching condition to the incident wave.

3.2. *Order* ε

Equation (3.12b) gives

$$S_{1\xi t} - \mathrm{i}S_{1\xi} = -\tfrac{1}{2}\left[\mathrm{e}^{2\mathrm{i}t}J(\mathrm{e}^{-\mathrm{i}x}\mathscr{S}, \mathrm{e}^{-\mathrm{i}x}\mathscr{S}_\xi) + J(\mathrm{e}^{\mathrm{i}x}\mathscr{S}^*, \mathrm{e}^{-\mathrm{i}x}\mathscr{S}_\xi)\right], \tag{3.17}$$

leading to

$$S_1 = \mathrm{i}\mathscr{R}(x, t, t_2) + \mathrm{e}^{2\mathrm{i}(t-x)}\left[\frac{1}{2}\mathscr{S}\mathscr{S}_\xi - \int_0^\xi \mathscr{S}_u^2\,\mathrm{d}u\right] + \frac{\mathscr{S}^*\mathscr{S}_\xi}{2}. \tag{3.18}$$

We satisfy the no-normal-flow condition (3.9a) by requiring that $\mathscr{R}$ is real. The no-slip condition (3.9b) and the no-flux condition (3.9c) are satisfied provided that $\mathscr{S}$ satisfies these conditions. At this order, the nonlinear effects produce a rectified and a second-harmonic waves.

Now we match (3.18) with (3.10). The most important result is that this matching condition defines the envelope of the nonlinearly reflected second harmonic:

$$\boxed{H(t_2) = -\int_0^\infty \mathscr{S}_\xi^{*2}\,\mathrm{d}\xi.} \tag{3.19}$$

Thus we have an expression for the amplitude of the second harmonic in terms of the incident wave. The matching tells also that $\mathscr{R} = H\mathrm{e}^{2\mathrm{i}(x-t)}(1 - \tilde{p}\sec\beta)/2\mathrm{i} + \text{c.c.}$ and that the rectified flow vanishes in the outer region because of condition (3.15).

3.3. *Order* ε^2

At this order, we have (3.12c). To avoid secular growth, all the resonant terms on the right-hand side must vanish. This condition determines the evolution equation for $\mathscr{S}(\xi, t_2)$.

Although it is not initially obvious, all nonlinear resonant contributions cancel† and the final evolution equation is *linear*:

$$\boxed{\mathscr{S}_{t_2\xi} - \mathrm{i}\sigma\mathscr{S}_{\xi} + \mathscr{S} - \varrho^2\mathscr{S}_{\xi\xi\xi} = A^*(t_2)}. \tag{3.20}$$

Using (3.20), one can obtain an alternative expression for the envelope of the second harmonic:

$$H_{t_2} + 2\mathrm{i}\sigma H = 2\varrho^2 \int_0^{\infty} \mathscr{S}^2_{\xi\xi}\,\mathrm{d}\xi - A^2. \tag{3.21}$$

We emphasize that although there are no nonlinear terms in (3.20), the nonlinearity is important for the generation of the second harmonic and also for all the nonlinear contributions to S_1 in (3.18). And when we come to visualize the solution, these nonlinearly forced components of the solution lead to a symmetry breaking.

Equation (3.20) is third order in space and we are imposing four boundary conditions in (3.15) and (3.16). Consequently, the problem is overspecified and we resolve this issue by discarding the no-buoyancy-flux condition $\mathscr{S}_{\xi\xi} = 0$. This unsatisfactory point might be corrected by demanding that the Péclet number in (2.11*b*) be very large. In this circumstance, one would expect a very thin buoyancy diffusive layer in which dynamics similar to that of Wunsch (1970) and Phillips (1970) is important.

4. The inviscid case

We first consider the special case of (3.20) in which the fluid is inviscid ($\varrho = 0$). The solution of (3.20) which satisfies the initial condition that $\mathscr{S}(\xi, 0) = 0$ is

$$\mathscr{S}(\xi, t_2) = \int_0^{t_2} A^*(t_2 - \tau)\mathrm{e}^{\mathrm{i}\sigma\tau}\sqrt{\frac{\xi}{\tau}}\, J_1\left(2\sqrt{\xi\tau}\right)\,\mathrm{d}\tau, \tag{4.1}$$

and (3.21) leads to the following expression for the envelope of the second harmonic:

$$H(t_2) = -\int_0^{t_2} \mathrm{e}^{2\mathrm{i}\sigma(\tau - t_2)}\, A^2(\tau)\,\mathrm{d}\tau. \tag{4.2}$$

The amplitude $A(t_2)$ of the incident wave must be specified to completely determine the solution. As in all the experiments, we take the simplest case in which $A(t_2)$ switches on suddenly at $t_2 = 0$ (Because A depends only on the slow time t_2, the sudden switch-on means that the incident wave achieves its ultimate constant amplitude on a time scale which is slow relative to t but fast relative to t_2). That is, $A(t_2) = 1$ when $t_2 > 0$.

4.1. *The critical case*

In the critical case $\sigma = 0$ the integral in (4.1) can be evaluated and

$$\mathscr{S} = 1 - J_0(2\sqrt{\xi t_2}), \tag{4.3}$$

where J_0 is the Bessel function of the first kind of order 0. Thus, in this critical case, the solution has a 'similarity' form in which the thickness of the inner region is inversely proportional to time. That is, there is no steady solution as $t \to \infty$. Instead, the disturbance near the slope becomes strongly oscillatory as the undulations of J_0 are intensified.

† The underlying reason for the miraculous cancellation of the resonant nonlinear terms is the following special case of the Jacobi identity: $J\left[\mathscr{Q}, J(\mathscr{Q}_{\xi}, \mathscr{Q}^*)\right] + J\left[\mathscr{Q}^*, J(\mathscr{Q}, \mathscr{Q}_{\xi})\right] + J\left[J(\mathscr{Q}, \mathscr{Q}^*), \mathscr{Q}_{\xi}\right] = 0$.

Using (4.3) we have

$$[\Psi_0, U_0] = \cos(x-t)\left[1-J_0, -2t_2\frac{J_1}{\chi}\right], \qquad (4.4a)$$

$$[W_0, P_0, B_0] = \sin(x-t)\left[J_0-1, 1+J_0, -2t_2\frac{J_1}{\chi}\right], \qquad (4.4b)$$

$$\Psi_1 = t_2\left(\frac{J_1}{\chi}(1-J_0)+J_0^2+J_1^2-1\right)\cos 2(x-t)+t_2(1-J_0)\frac{J_1}{\chi}, \qquad (4.4c)$$

$$U_1 = 2t_2^2\left(\frac{J_2(1-J_0)+J_1^2}{\chi^2}\right)\cos 2(x-t)+2t_2^2\left(\frac{J_2}{\chi^2}(1-J_0)-\frac{J_1^2}{\chi^2}\right), \qquad (4.4d)$$

$$W_1 = 2t_2\left(1-J_0^2-J_1^2-\frac{J_1}{\chi}(1-J_0)\right)\sin 2(x-t), \qquad (4.4e)$$

$$B_1 = 2t_2^2\left(\frac{J_2}{\chi^2}(1-J_0)+\frac{J_1^2}{\chi^2}\right)\sin 2(x-t), \qquad (4.4f)$$

where $\chi \equiv 2\sqrt{\xi t_2}$ and $J_i = J_i(\chi)$. Notice that in this critical case the alongslope velocity U_0 and the buoyancy perturbation B_0 both grow linearly with time. This response is analogous to that of a resonantly forced oscillator.

The streamfunction is shown in figure 5. At small times the reflection process creates a regular array of counter-rotating vortices. As time progresses, figure 5(*b*) shows that the scale of the vortices decreases. Panels (*c*) and (*d*) are both at $N\sin\beta\ t = 3$. The 'velocity vector' presentation in panel (*d*) more clearly displays the asymmetry of the vortices which is the effect of the nonlinear terms in Ψ_1.

Figure 6 shows the distortion of the isopycnals as the oscillations amplify. In panel (*a*) the disturbance is very small and one sees essentially the initial background stratification. In panel (*b*) the disturbance begins to 'fold-up' the isopycnals and, near the slope, this process produces a region of static instability. In the panel (*c*) the development of small scales in the isopycnal field is evident.

In this case, with $\sigma = 0$, the amplitude of the second harmonic is a linear function of time:

$$H(t_2) = -t_2 = -\frac{\varepsilon^2}{\tan\gamma}\ t, \qquad (4.5)$$

and so $\varepsilon\Psi_1$ becomes comparable to Ψ_0 when $t_2 = O(\varepsilon^{-1})$. For these reasons the expansion becomes disordered when $t_2 = O(\varepsilon^{-1})$ and the results above are no longer reliable. However, as we show below, well before this breakdown, the buoyancy becomes statically unstable. Thus the expansion above strongly suggests that the next evolutionary stage is characterized by the onset of turbulence triggered by overturning instability.

4.2. *Overturning instability or stratified shear flow instability?*

One scenario for the transition to turbulence is that the growing disturbance produces a statically unstable density field which then overturns (we refer this as overturning instability). An alternative is that the local Richardson number might fall below a critical value while the density is still statically stable. In this second case the overturns are produced by a rapidly growing secondary shear flow instability. Experimentally,

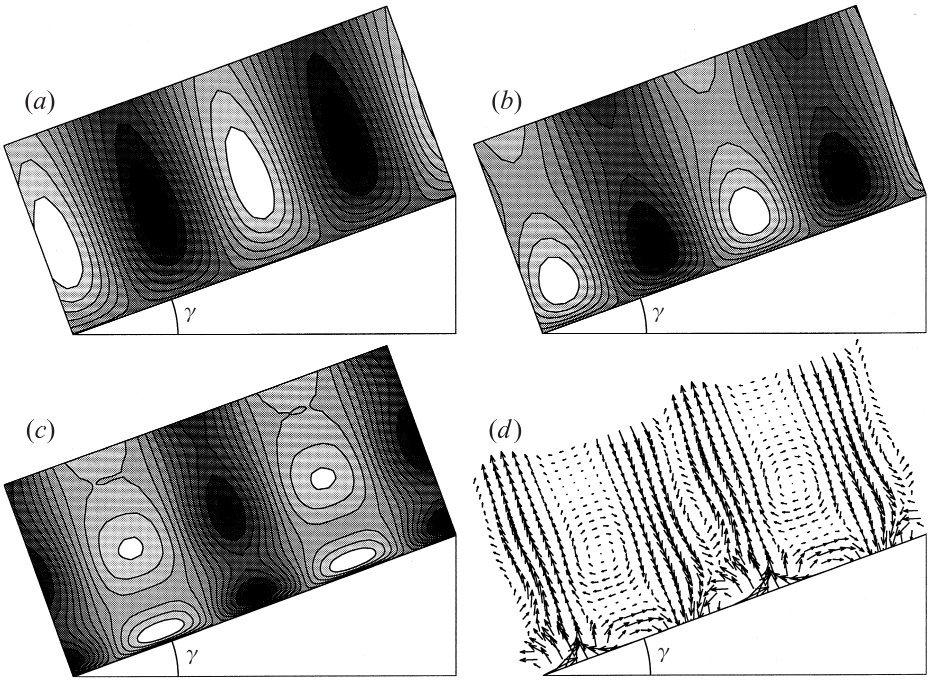

FIGURE 5. Streamfunction for four different times in the critical case. (a–c) $N \sin\beta\ t = \frac{1}{2}$, 1 and 3. (d) An alternative 'velocity vector' visualization of (c). $\varepsilon = 0.3$, $\gamma = \beta = 20°$. In (d), there are two pairs of counter-rotating vortices immediately adjacent to the slope. The clockwise vortices are slower and thinner than the counter-clockwise vortices. This symmetry breaking is a result of the second-harmonic term such as Ψ_1 in (4.4). The dimensions of the panel are $2\lambda/\sin\alpha$ in the x-direction (i.e. two alongslope wavelengths) by $\lambda/\sin\alpha$ in the z-direction.

Thorpe & Haines (1987) have reported that the overturning instability is very likely to be convectively driven. On the other hand, Slinn & Riley (1998*a*) identified a shear instability mechanism; but they noted that the Reynolds number of their numerical simulations was matched to experimental values by forcing larger amplitude waves in a more viscous fluid. Consequently, the Richardson number in these simulations was relatively low compared to those of laboratory experiments. However, all these claims must be viewed cautiously because both instabilities are intrinsically related in a stratified flow.

Using our analytic results we can make a rough assessment of these two possibilities. Taking into account the background linear buoyancy, and the first-order correction, we can calculate the overturning time t_o which is the time at which negative vertical buoyancy gradients first occur. In dimensional variables:

$$t_o = \frac{\sqrt{8\tan\gamma}}{N\sin 2\gamma}\,\varepsilon^{-3/2}. \tag{4.6}$$

We can also calculate the time t_s at which the minimum Richardson number first falls below 1/4:

$$t_s = \sqrt{\frac{2}{\cos\gamma}}\,t_o > t_o. \tag{4.7}$$

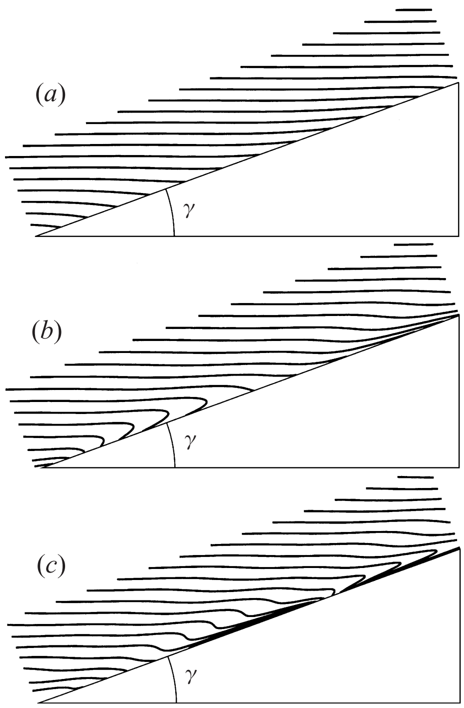

FIGURE 6. (a–c) Buoyancy field in the critical case at $N \sin\beta\ t = 3$, 10 and 20. $\varepsilon = 0.3$; $\beta = \gamma = 20°$. The dimensions of the panel are $\lambda/\sin\alpha$ in the x-direction by $\lambda/5\sin\alpha$ in the z-direction. In (b) and (c), some overturned regions are evident.

This analytical calculation also shows that both of the unstable conditions above occur first at the wall (see also Jevam *et al.* 1997).

Because $t_o < t_s$ we can argue that the convectively driven overturning instability should appear first. In the typical experimental case $\varepsilon = 0.3$, for example, both critical times are plotted as a function of the slope angle γ in figure 7. It is interesting to note that $N \sin\beta\ t_o$ is an increasing function of the slope angle γ.

However, let us note that the domain of validity of the Miles–Howard theorem (stability if $Ri > 1/4$) applies to steady, parallel shear flows, whereas the present flow is unsteady and non-parallel. In addition, (4.7) was derived using the usual definition of the Richardson number $Ri = N^2/U_z^2$ (see, for example, Kundu 1990). An alternative definition could be

$$\tilde{Ri} = -\frac{(g/\rho_0)\mathrm{d}\rho/\mathrm{d}z}{U_z^2}, \tag{4.8}$$

where the numerator takes into account not only the background buoyancy, but also the perturbative part of the buoyancy. It is clear from (4.8), that $\tilde{Ri}$ would reach 1/4 before zero, and therefore before negative vertical buoyancy gradients first occur. So, the whole discussion simply indicates that there are plausible reasons to expect that the solution we have found will become unstable, and ultimately turbulent, and we have *three* criteria for instability; the static instability time is sandwiched between the $\tilde{Ri} = 1/4$ and $Ri = 1/4$ times.

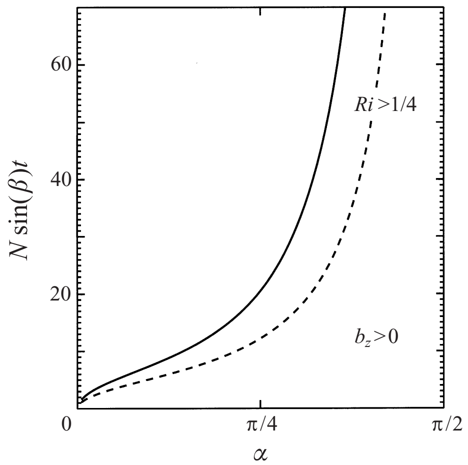

FIGURE 7. $N \sin\beta\ t_o$ (dashed line) and $N \sin\beta\ t_s$ (solid line) as a function of the slope angle γ. $\varepsilon = 0.3$.

4.3. *The non-critical case*

We now turn to the case in which the incident wave is not precisely critical so that $\sigma \neq 0$. We continue with the assumption that the fluid is inviscid ($\varrho = 0$) and that the incident wave envelope is $A(t_2) = 1$ if $t_2 > 0$.

In this case (3.20) has a steady solution which satisfies the boundary condition at $\xi = 0$:

$$\mathscr{S} = 1 - \mathrm{e}^{-\mathrm{i}\xi/\sigma}. \tag{4.9}$$

This steady solution is an approximate version of the linearly reflected wave identified by Phillips (1966). Notice how the scale of the oscillations is reduced as $\sigma \to 0$. Thus, when the incidence is nearly critical, one expects to see an initial reduction in scale which is the t^{-1} behaviour identified in (3.20). But this scale reduction is arrested at time $t_2 = O(1/|\sigma|)$ when the Phillips solution in (4.9) is established as a steady state.

In order to understand the details of how the steady solution in (4.9) emerges we can use the solution of the initial value problem given in (4.1):

$$\mathscr{S} = \int_0^{2\sqrt{\xi t_2}} \mathrm{e}^{\mathrm{i}\sigma u^2/4\xi} J_1(u)\,\mathrm{d}u, \tag{4.10a}$$

$$[\Psi_0, W_0] = [\mathrm{Re}, \mathrm{Im}] \int_0^{2\sqrt{\xi t_2}} J_1(u)\,\mathrm{e}^{\mathrm{i}(t+(\sigma u^2/4\xi)-x)}\,\mathrm{d}u, \tag{4.10b}$$

$$[U_0, B_0] = [-\mathrm{Re}, \mathrm{Im}] \int_0^{t_2} J_0(2\sqrt{\xi\tau})\mathrm{e}^{\mathrm{i}(t+\sigma\tau-x)}\,\mathrm{d}\tau, \tag{4.10c}$$

$$[U_1, B_1] = \tfrac{1}{2}[-\mathrm{Re}, \mathrm{Im}][\mathrm{e}^{2\mathrm{i}(t-x)}\left(\mathscr{S}\mathscr{S}_{\xi\xi} - \mathscr{S}_\xi^2\right) + \left(\mathscr{S}^\star \mathscr{S}_\xi\right)_\xi], \tag{4.10d}$$

$$H = -\sigma^{-1} \sin\sigma t_2\ \mathrm{e}^{-\mathrm{i}\sigma t_2}. \tag{4.10e}$$

At early times, the streamfunction in figure 8 is similar to the critical case in figure 5. However, as time progresses, the steady solution in (4.9) is set up first in the neighbourhood of the wall, and then this cellular pattern expands outwards. Figure 9 shows that the region in which the flow becomes steady is characterized by regular pattern of vortices. Figure 10 shows the isopycnals at a given time: the

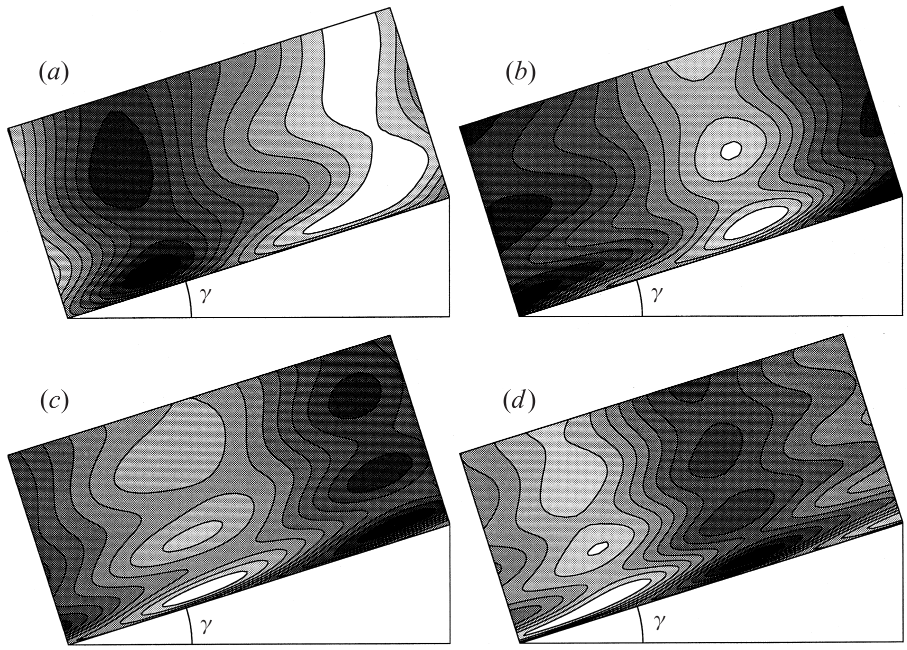

FIGURE 8. Streamfunction for four different times in the near-critical case: $\beta = 22.58°$; $\gamma = 17.42°$; $\sigma = -1$; $\varepsilon = 0.3$. (a–d) $N \sin\beta\ t = 5$, 10, 15 and 20. The dimensions of the panel are $\lambda/\sin\alpha$ in the x-direction by $\lambda/2\sin\alpha$ in the z-direction.

pattern is similar to experimental results reported in figure 12 of Thorpe (1987) (see also McPhee 1998).

As in the critical case, one can compute t_o and t_s for different values of σ. Again, the instability is convectively driven and initiated at the wall; t_o is plotted in figure 11 as a function of the slope angle γ for different values of σ. An interesting point is that, for a given value of γ, the positive values of σ leads to an earlier appearance of the instability. This point is rationalized by noticing that, once γ is given, a positive σ corresponds to a smaller value for α. As the expression (4.6) is an increasing value of the angle $\alpha = 2\gamma$, near-critical up-slope (respectively downslope) reflections are unstable slightly before (respectively after) critical reflections. Indeed, plotted as a function of α, t_o and t_s are almost independent of σ.

This is consistent with the observations reported by De Silva *et al.* (1997) that for moderately supercritical waves the instabilities developed near the bed. They have, however, also studied experimentally the variation of the boundary layer thickness as the incident waves become far from critical, and their results show that the instability is initiated away from the bed. In the framework of this near-critical reflection theory (i.e. for small values of ε and σ), we found that the wave overturning always starts on the slope; however as time continues the unstable region extends away from the boundary (for example, see the unstable region in figure 10). For strongly subcritical and supercritical cases, internal wave reflection from the sloping bed should be interpreted as wave–wave interaction between the incident and the reflected waves since, as shown by De Silva *et al.* (1997), the area of interaction region increases progressively as the waves depart from critical condition.

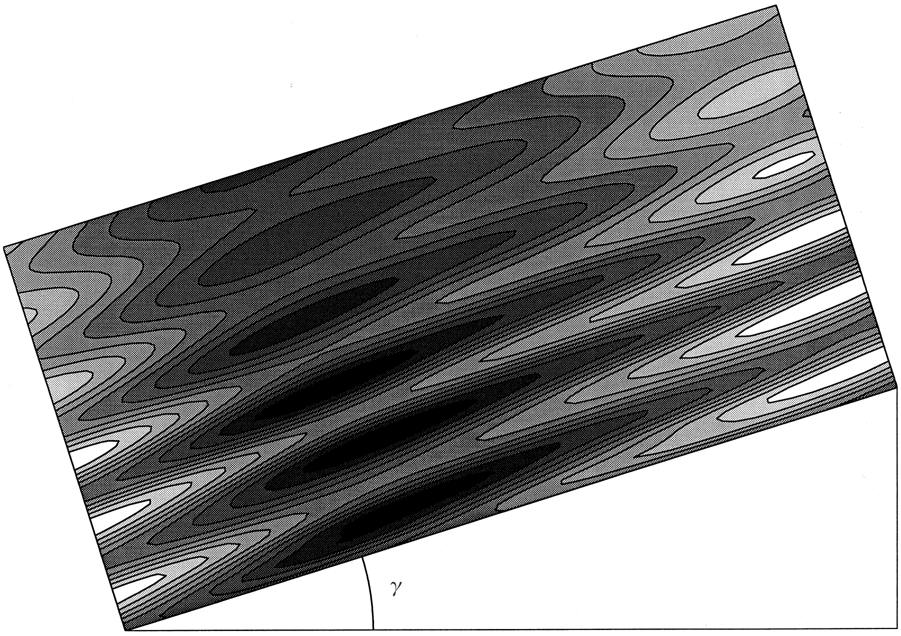

FIGURE 9. Streamfunction in the near-critical case at $N \sin\beta\ t = 100$: $\beta = 22.58°$; $\gamma = 17.42°$; $\sigma = -1$; $\varepsilon = 0.3$. The dimensions of the panel are $\lambda/\sin\alpha$ in the x-direction by $\lambda/2\sin\alpha$ in the z-direction.

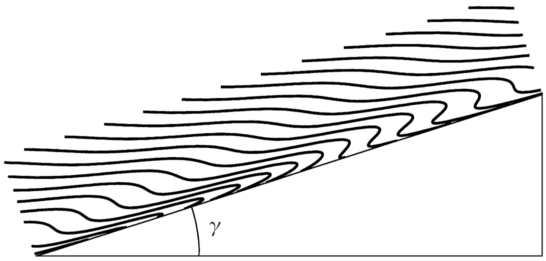

FIGURE 10. Buoyancy field at $N \sin\beta\ t = 20$ in the near-critical case $\beta = 22.58°$; $\gamma = 17.42°$ and $\varepsilon = 0.3$. The dimensions of the panel are $\lambda/\sin\alpha$ in the x-direction by $\lambda/5\sin\alpha$ in the z-direction.

5. Viscous effects

In the viscous case, $\varrho \neq 0$, there is a steady solution of (3.20) even if the forcing is precisely critical. For the sake of simplicity, consider the case in which $\varrho \neq 0$, $\sigma = 0$, and the incident wave envelope is $A(t_2) = 1$ if $t_2 > 0$ (this is a typical experimental switch on). The steady solution of (3.20) which satisfies the no-mass-flux and no-slip boundary conditions at $\xi = 0$ is analogous to the western meridional boundary layer, also called the Munk layer (see for example Pedlosky 1987). It reads

$$\mathscr{S} = 1 - \frac{2}{\sqrt{3}} \sin\left(\frac{\sqrt{3}\xi}{2\varrho^{2/3}} + \frac{\pi}{3}\right) \mathrm{e}^{-\xi/2\varrho^{2/3}} \tag{5.1}$$

(we continue to assume that $\kappa = 0$ and discard the no-buoyancy-flux boundary condition at $\xi = 0$). The solution above, presented in figure 12 in the extremely viscous case $\ell = 1$, shows that $2\varrho^{2/3}$ is the viscous boundary layer thickness in the

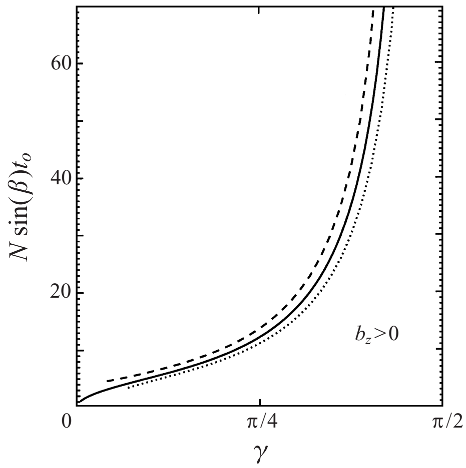

FIGURE 11. $N \sin\beta\ t_o$ against the slope angle γ. $\sigma = 0$ (solid curve), $\sigma = 1$ (dotted curve), $\sigma = -1$ (dashed curve). $\varepsilon = 0.3$.

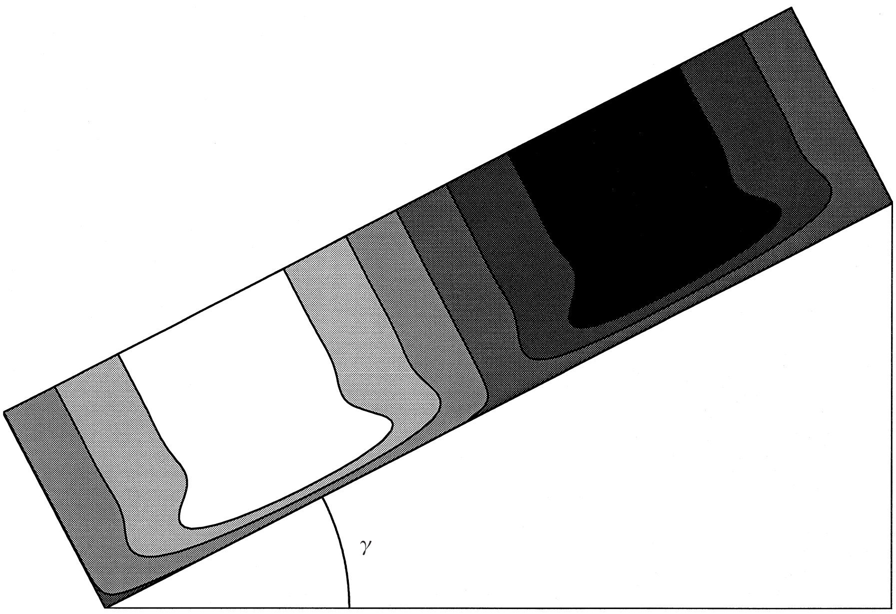

FIGURE 12. Final steady-state solution in the critical case: $\beta = 32.58°$; $\gamma = 27.42°$; $\sigma = -1$; $\varepsilon = 0.3$. The dimensions of the panel are $\lambda/\sin\alpha$ in the x-direction by $\lambda/4\sin\alpha$ in the z-direction.

terms of ξ; in dimensional variables this boundary layer thickness is

$$\ell = \left(\frac{\nu + \kappa}{KN\sin\beta}\right)^{1/3}\left(\frac{4}{1+\cos\alpha}\right)^{1/3}. \tag{5.2}$$

Thus, in the steady state, the viscous boundary layer thickness is a decreasing function of the slope angle.

The steady-state solution is probably irrelevant in many experimental systems because $\varrho \ll 1$ (see table 1) and one expects that turbulent transition occurs before the steady state is approached. In this case with $\varrho \ll 1$, we can again use asymptotic

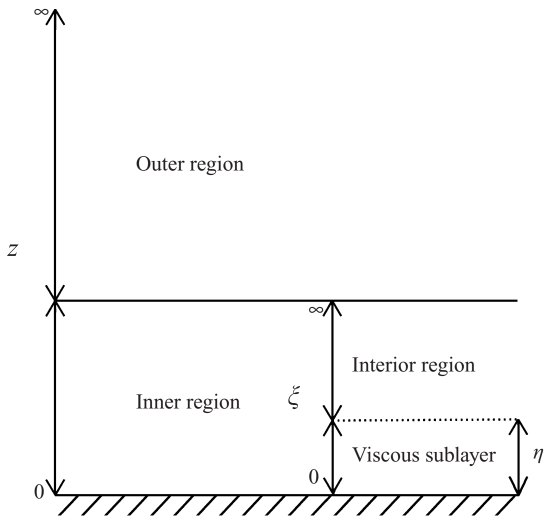

FIGURE 13. Schematic view of the different regions used in the matched asymptotic expansion.

matching to develop an approximate solution of the initial value problem. There is an interior region in which the effect of viscosity is small and the solution is approximated by (4.1). However this interior solution of §4 does not satisfy the no-slip condition and so it is necessary to include a viscous sublayer close to the topography (see figure 13 for a schematic representation of the different regions).

The details of this matching problem are in the Appendix. The solution in the interior region is

$$\mathscr{S}(\xi,t_2)=\int_0^{t_2} A^*(t_2-\tau)\,\mathrm{e}^{\mathrm{i}\sigma\tau}\sqrt{\frac{\xi}{\tau}}\,J_1\left(2\sqrt{\xi\tau}\right)\,\mathrm{d}\tau$$
$$+\varrho\int_0^{t_2}\left(\mathscr{S}'_{1\star}(t_2-\tau)-\mathrm{i}\sigma\mathscr{S}_{1\star}(t_2-\tau)\right)J_0\left(2\sqrt{\xi\tau}\right)\,\mathrm{d}\tau+O(\varrho^2) \quad (5.3)$$

where

$$\mathscr{S}_{1\star}(t_2)=-\frac{2}{\sqrt{\pi}}\int_0^{t_2}\sqrt{t_2-\tau}\;\mathrm{e}^{\mathrm{i}\sigma(t_2-\tau)}\,A^*(\tau)\mathrm{d}\tau \quad (5.4)$$

and J_0 is the Bessel function of the first kind of order 0.

In the viscous sublayer the solution is

$$\mathscr{S}(\xi,t_2)=\xi\int_0^{t_2}\mathrm{e}^{\mathrm{i}\sigma(t_2-\tau)}A^*(\tau)\,\mathrm{d}\tau$$
$$+\varrho\left[\mathscr{S}_{1\star}(\xi,t_2)+\int_0^{t_2}\mathrm{d}u\frac{\mathrm{e}^{-\xi^2/4\varrho^2u}}{\sqrt{\pi u}}\int_0^{t_2-u}A^*(\tau)\mathrm{e}^{\mathrm{i}\sigma(t_2-\tau)}\mathrm{d}\tau\right]+O(\varrho^2). \quad (5.5)$$

In the critical case with $\sigma=0$ and $A(t_2)=1$, if $t_2>1$, the integrals above can be simplified. The interior solution is

$$\mathscr{S}(\xi,t_2)=1-J_0(2\sqrt{\xi t_2})-\frac{\varrho}{2\sqrt{\pi}\xi^{3/2}}\left(\sin 2\sqrt{\xi t_2}-2\sqrt{\xi t_2}\cos 2\sqrt{\xi t_2}\right)+O(\varrho^2) \quad (5.6)$$

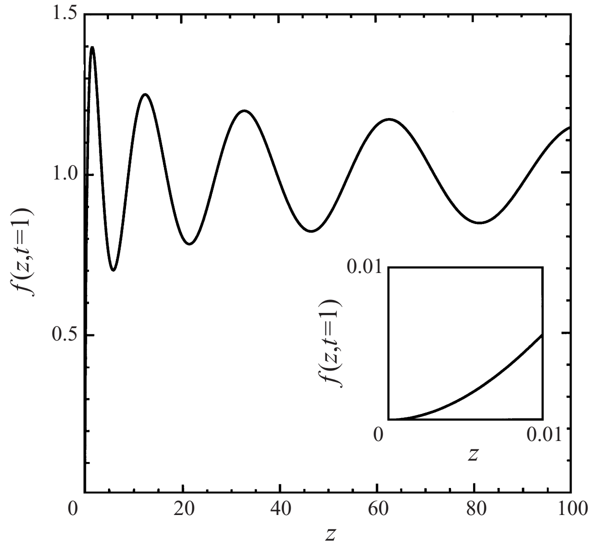

FIGURE 14. Function f against the distance normal to the slope z at time $t = 1$ and for $\varrho = 0.1$, in the critical case. In the inset, we plot the viscous sublayer solution valid only very close to the wall, i.e. $z \ll 1$.

and in the viscous sublayer, the solution is

$$\mathscr{S}(\xi, t_2) = \xi t_2 - \frac{\varrho t_2^{3/2}}{\sqrt{\pi}} \left[\frac{4}{3} + \int_0^1 \mathrm{d}u \frac{u-1}{\sqrt{u}} \, \mathrm{e}^{-\xi^2/4\varrho^2 t_2 u} \right] + O(\varrho^2). \tag{5.7}$$

Both functions are plotted against z in figure 14 in the typical case $\varrho = 0.1$ and $\varepsilon = 0.3$. It is clear that the region where the viscous effects are important corresponds only to a very thin region along the slope.

6. Conclusion and discussion

The thrust of this paper has been to study the weakly nonlinear and nearly critical incidence of internal waves onto a slope. The scalings of §§ 2 and 3 amount to taking the distinguished limit $|\beta - \gamma| \to 0$ with $a \propto |\beta - \gamma|^{3/2}$ (a is the amplitude parameter in (2.12)). At leading order, these assumptions give the linear oscillator equation (3.12*a*) in which the coordinate normal to the slope, ξ, appears only parametrically. Thus, the buoyancy oscillations along the slope are uncoupled at leading order. The weak coupling between oscillations at different ξ is uncovered by higher orders in the expansion scheme and is apparent in the forced dispersive wave equation (3.20). One can then view the incident internal wave as a nearly resonant forcing of this continuum of weakly coupled (and weakly damped if $\varrho \neq 0$) oscillators.

The scenario above describes the initial evolutionary stages of nearly critical incidence. However the limitations of this approach become apparent when the oscillations become so extreme that they either overturn the buoyancy field, or strongly violate the Miles–Howard stability condition (see figure 6*c*). In either case, we expect a rapid transition to turbulence, dramatically enhanced mixing in the neighbourhood of the slope, and the production of intrusive layers (e.g. Ivey & Nokes 1989; De Silva 1997; McPhee 1998).

Within the present framework the most interesting complication that can be included is *oblique* incidence. Experimental data by Eriksen (1998) and theoretical work by Thorpe (1997) have recently emphasized the importance of alongslope currents in the reflection process for obliquely incident waves in a uniformly stratified rotating fluid. We speculate that the weakly nonlinear term will have interesting consequences, such as mean flow induction, if the incidence is oblique.

We thank Angel Alastuey, Neil Balmforth, Paola Cessi, Erika McPhee, Florence Raynal and S. A. Thorpe for helpful conversations. We also thank three anonymous referees for their thoughtful review of this manuscript. This research was supported by the National Science Foundation under award OCE96-16017 with additional support for TD by a NATO fellowship. The laboratoire de Physique de l'Ecole Normale Supérieure de Lyon is UMR-CNRS-5672.

Appendix. Derivation of the solution in the viscous case

Defining

$$f(\xi, t_2) = \mathscr{S}(\xi, t_2)\, \mathrm{e}^{-\mathrm{i}\sigma t_2} \quad \text{and} \quad g(t_2) = A^*(t_2)\, \mathrm{e}^{-\mathrm{i}\sigma t_2}, \qquad (\text{A } 1a, b)$$

(3.20) becomes

$$f_{t_2\xi} + f - \varrho^2 f_{\xi\xi\xi} = g \qquad (\text{A } 2)$$

with the four conditions

$$f(0, t_2) = f_\xi(0, t_2) = f_{\xi\xi}(0, t_2) = 0 \quad \text{and} \quad \lim_{\xi \to \infty} f(\xi, t_2) = g(t_2). \qquad (\text{A } 3a\text{–}d)$$

A.1. *Interior region*

In the interior region, the solution of (A 2) is obtained by expanding f in powers of ϱ:

$$f(\xi, t_2) = f_0(\xi, t_2) + \varrho\, f_1(\xi, t_2) + O(\varrho^2). \qquad (\text{A } 4)$$

The substitution of (A 4) into (A 2) leads to the following hierarchy:

$$\varrho^0: \quad f_{0t_2\xi} + f_0 = g, \qquad (\text{A } 5a)$$

$$\varrho^1: \quad f_{1t_2\xi} + f_1 = 0. \qquad (\text{A } 5b)$$

At leading order, ϱ^0, the solution of (A 5*a*) should satisfy the two conditions

$$f_0(0, t_2) = 0 \quad \text{and} \quad \lim_{\xi \to \infty} f_0(\xi, t_2) = g(t_2). \qquad (\text{A } 6a, b)$$

The solution can be obtained using the Laplace transform and we get

$$f_0(\xi, t_2) = \int_0^{t_2} g(t_2 - \tau) \sqrt{\frac{\xi}{\tau}}\, J_1\left(2\sqrt{\xi\tau}\right)\, \mathrm{d}\tau \qquad (\text{A } 7)$$

where J_1 is the Bessel function of the first kind of order 1.

At order ϱ, (A 5*b*) with the conditions

$$f_1(0, t_2) = f_{1\star}(t_2) \quad \text{and} \quad \lim_{\xi \to \infty} f_1(\xi, t_2) = 0, \qquad (\text{A } 8a, b)$$

leads to the solution

$$f_1(\xi, t_2) = \int_0^{t_2} f_{1\star}'(t_2 - \tau)\, J_0\left(2\sqrt{\xi\tau}\right)\, \mathrm{d}\tau. \qquad (\text{A } 9)$$

The unknown function $f_{1\star}(t_2)$ will be determined by matching the viscous sublayer solution.

A.2. *Viscous sublayer*

In the viscous sublayer, using the stretched coordinate $\eta = \xi/\varrho$ and $h(\eta, t_2) = f(\xi, t_2)/\varrho$, (A 2) becomes

$$h_{t_2\eta} - h_{\eta\eta\eta} + \varrho\, h = g. \tag{A 10}$$

Expanding h in powers of ϱ, the leading-order solution is

$$h_0(\eta, t_2) = f_{1\star}(t_2) + \eta \int_0^{t_2} g(\tau)\mathrm{d}\tau + r(\eta, t_2), \tag{A 11}$$

where $r(\eta, t_2)$ satisfies the diffusion equation

$$r_{t_2} = r_{\eta\eta}, \tag{A 12}$$

with the three conditions

$$r_\eta(0, t_2) = -\int_0^{t_2} g(\tau)\mathrm{d}\tau, \quad \lim_{\xi\to\infty} r = 0 \quad \text{and} \quad r(0, t_2) = -f_{1\star}(t_2). \tag{A 13a–c}$$

Let us stress that the two first conditions define completely the solution of (A 12), whereas the last one determines $f_{1\star}(t_2)$ in terms of $g(t_2)$.

Using the Laplace transform, one obtains the solution of (A 12) and we finally get not only the function

$$f_{1\star}(t_2) = -\frac{2}{\sqrt{\pi}} \int_0^{t_2} \sqrt{t_2 - \tau}\; g(\tau)\mathrm{d}\tau \tag{A 14}$$

but also the the general solution in the viscous sublayer given by

$$f(\xi, t_2) = \xi \int_0^{t_2} g(\tau)\mathrm{d}\tau + \varrho \left[f_{1\star}(t_2) + \int_0^{t_2} \mathrm{d}u\, \frac{\mathrm{e}^{-\xi^2/4\varrho^2 u}}{\sqrt{\pi u}} \int_0^{t_2-u} g(\tau)\mathrm{d}\tau \right] + O(\varrho^2). \tag{A 15}$$

REFERENCES

Armi, L. 1978 Some evidence of boundary mixing in the deep ocean. *J. Geophys. Res.* **83**, 1971–1979.

Cacchione, D. & Wunsch, C. 1974 Experimental study of internal waves over a slope. *J. Fluid Mech.* **66**, 223–239.

Caldwell, D. R., Brubaker, J. M. & Neal, V. T. 1978 Thermal microstructure on a lake slope. *Limnol. Oceanogr.* **23**, 372.

De Silva, I. P. D., Imberger, J. & Ivey, G. N. 1997 Localized mixing due to a breaking internal wave ray at a sloping bed. *J. Fluid Mech.* **350**, 1–27.

Eriksen, C. C. 1978 Measurements and model of fine structure, internal gravity waves and wave breaking in the deep ocean. *J. Geophys. Res.* **83**, 2989–3009.

Eriksen, C. C. 1982 Observations of internal wave reflection off sloping bottoms. *J. Geophys. Res.* **87**, 525–538.

Eriksen, C. C. 1985 Implications of ocean bottom reflection for internal wave spectra and mixing. *J. Phys. Oceanogr.* **15**, 1145–1156.

Eriksen, C. C. 1998 Internal wave reflection and mixing at Fieberling Guyot. *J. Geophys. Res.* **103**, 2977–2994.

Garett, C. & Munk, W. 1979 Internal waves in the ocean. *Ann. Rev. Fluid Mech.* **11**, 339–369.

Gilbert, D. 1993 A search for evidence of critical internal wave reflection on the continental rise and slope off Nova Scotia. *Atmos.-Ocean* **31**, 99–122.

Gilbert, D. & Garrett, C. 1989 Implications for Ocean Mixing of internal wave scattering off irregular topography. *J. Phys Oceanogr.* **19**, 1716–1729.

Ivey, G. N. & Nokes, R. I. 1989 Vertical mixing due to the breaking of critical internal waves on sloping boundaries. *J. Fluid Mech.* **204**, 479–500.

JAVAM, A., IMBERGER, J. & ARMFIELD, A. 1997 Numerical study of internal wave breaking on a sloping boundary. *J. Fluid Mech.* (submitted).

KUNDU, P. K. 1990 *Fluid Dynamics*. Academic Press.

MCPHEE, E. E. 1998 http://www.ocean.washington.edu/people/grads/eemcphee/mcphee.html.

MUNK, W. 1966 Abyssal recipes. *Deep-Sea Res.* **13**, 707–730.

MUNK, W. H. 1981 Internal waves and small-scale processes. In *Evolution of Physical Oceanography. Scientific Surveys in Honor of Henry Stommel* (ed. B. Warren & C. Wunsch) pp. 264–291. MIT Press.

PEDLOSKY, J. 1987 *Geophysical Fluid Dynamics*. Springer.

PHILLIPS, O. M. 1966 *The Dynamics of the Upper Ocean*. Cambridge University Press.

PHILLIPS, O. M. 1970 On flows induced by diffusion in a stably stratified fluid. *Deep-Sea Res.* **17**, 435–443.

POLZIN, K. L., TOOLE, J. M., LEDWELL, J. R. & SCHMITT, R. W. 1997 Spatial variability of turbulent mixing in the abyssal ocean. *Science* **76**, 93–96.

SANDSTROM, H. 1966 The importance of topography in generation and propagation of internal waves. PhD Thesis, University of California, San Diego.

SLINN, D. N. & RILEY, J. J. 1996 Turbulent mixing in the oceanic boundary layer caused by internal wave reflection from sloping terrain. *Dyn. Atmos. Oceans* **24**, 51–62.

SLINN, D. N. & RILEY, J. J. 1998*a* Turbulent dynamics of a critically reflecting internal gravity wave. *Theor. Comput. Fluid Dyn.* (in press).

SLINN, D. N. & RILEY, J. J. 1998*b* Internal wave reflection from sloping boundaries. *J. Fluid Mech.* (submitted).

TAYLOR, J. R. 1993 Turbulence and mixing in the boundary layer generated by shoaling internal waves. *Dyn. Atmos. Oceans.* **19**, 233–258.

THORPE, S. A. 1987 On the reflection of a strain of finite-amplitude internal waves from a uniform slope. *J. Fluid Mech.* **178**, 279–302.

THORPE, S. A. 1997 On the interactions of internal waves reflecting from slopes. *J. Phys. Oceanogr.* **27**, 2072–2078.

THORPE, S. A. & HAINES, A. P. 1987 Appendix to On the reflection of a strain of finite-amplitude internal waves from a uniform slope. *J. Fluid Mech.* **178**, 299–302.

WUNSCH, C. 1970 On oceanic boundary mixing. *Deep-Sea Res.* **17**, 293–301.